IOSR Journal Of Applied Geology And Geophysics (IOSR-JAGG)
E-ISSN: 2321–0990, P-ISSN: 2321–0982.Volume 12, Issue 5 Ser. I (Sept. – Oct. 2024), 35-52
Www.Iosrjournals.Org

VSP Modeling With The Reflectivity Method And Semblance Processing

L. W. B. Leite, W. W. S. Vieira, A. D. S. Ferreira, F. T. B. Andrade
Faculty Of Geophysics, Federal University Of Pará (UFPA), Brazil

Abstract:
The present work deals with a specific detail of the VSP technique for estimating local compressional, v_P, and shear, v_S, wave velocities focused on reservoir characterization and seismic interpretation in sedimentary basins. This investigation was based on the presence of fluids (water, oil, gas) in porous rocks and its relationship with the $\gamma = \frac{v_S}{v_P}$ ratio, which mainly affects the shear wave velocity. The forward modeling was based on the reflectivity method to simulate seismic sections along depth in the borehole, considering the presence of a reservoir formation with an anomalous γ ratio value. The seismic processing of the vertical, transversal, and radial components produced by VSP modeling was based on band-pass filtering for upward and downward field separation, semblance picking, and NMO correction for estimating v_P and v_S wave velocities. Additionally, we compare different semblance measures to validate the NMO correction. The results show an accurate estimate of the γ ratio in the target layer, even considering receivers at different depths and high noise levels in the VSP sections. Besides that, the 2D numerical experiment reveals information about the sensitivity of the γ parameter in a layered medium with velocity variation, principally around regions with the potential presence of oil and gas.

Keywords: *VSP modeling, VSP processing, sedimentary basin modeling, pressure prediction, subsurface stress.*

Date of Submission: 02-11-2024 Date of Acceptance: 12-11-2024

I. Introduction

This research work is part of a major academic project for the prediction of subsurface stress using $v_{\mathrm{P}}(\mathbf{x})$ and $v_{\mathrm{S}}(\mathbf{x})$ velocities and density $\rho(\mathbf{x})$ to image low- and high-pressure zones that act as natural suction pumps between productive and reservoir layers, towards oil and gas exploration. Our specific goal in this article is to conduct a computational experiment to investigate the possibility of measuring the $v_{\mathrm{P}}(\mathbf{x})$ and $v_{\mathrm{S}}(\mathbf{x})$ velocities to discriminate the $\gamma = \frac{v_{\mathrm{S}}(\mathbf{x})}{v_{\mathrm{P}}(\mathbf{x})}$ ratio looking for an anomalous value. The thesis is based on the relationship between the γ ratio and the presence of fluids (water, oil, gas) in porous rocks affecting the S-wave more than the P-wave velocity, as presented by Sibiryakov [32]. Therefore, we could promote a further practical analysis of this relationship on simulated borehole data using the reflectivity methods.

The major part of the seismic exploration methods is based on the acoustic wave equation, which results in the knowledge of a $v_{\mathrm{P}}(\mathbf{x})$ distribution. Since the required data for pressure prediction includes $v_{\mathrm{S}}(\mathbf{x})$ and $\rho(\mathbf{x})$ distributions, three-component sensors (3C) can be used to obtain P and S (SH and SV) wave modes. Density log information can be incorporated, as tables and regression methods for incorporating seismic velocities and densities in rock pressure prediction studies.

Shear wave velocities can also be obtained from VSP technology, and petrophysical measurements [18, 6, 12]. Special issues related to the γ ratio of multicomponent VSP have been reported by O'Brian and Harris [27]. Gregory [14]'s work is outstanding and a major reference here, where he investigated the dependencies of P and S waves velocities for water-saturated porous reservoirs, as described by Sibiryakov et al. [32], and we follow with a short description about the topic on anomalous γ ratio to justify our efforts.

Vertical Seismic Profiling (VSP) represents a classical methodology to obtain $v_{\mathrm{P}}(\mathbf{x})$ and $v_{\mathrm{S}}(\mathbf{x})$ velocities information in a specific depth window, considering that there is a model control for the geometry of the interfaces, as classically described by Galperin [12] and Hardage [17], among several others.

It is rather usual to apply ray theory and tracing for VSP modeling, where complex geology and trajectories can be exhaustively applied. This specific study incorporates the reflectivity method, where the geometrical and physical model is the same used for stack and migration processes; in other words, a layered half-space composed of homogeneous and isotropic layers.

The study is based on two vertical trajectories between source and receiver along the borehole: first, the direct wave downwards informing the average velocity of the overburden; second, the reflection from the bottom of the target zone, informing the desired local velocity of the target medium interval. An important piece of information is that, for the shown experiments, the distance between the source and the borehole top is small enough to consider the trajectory as zero-offset.

A little more general geological and physical description would consider gentle dipping layers, a marine water layer on the top of a pack of sedimentary layers resting on a metamorphic basement, the P-S scattering in the elastic medium, the reverberation process of the borehole fluid, anisotropy, and ambient noise. Several aspects of VSP make it attractive, and one of them is due to the receiver's proximity to a potential reservoir; besides, ray trajectory is considered to have less distortion concerning surface methods and with less interference from lateral variations of the upper layers.

The major propagation energy observed in a borehole environment is P and S waves, as upgoing and downgoing modes and their conversions, exhibiting spherical spreading and the so-called tube waves that travel along the cylindrical fluid-solid boundary at a low and almost fixed velocity without exhibiting spherical spreading, and we can also add the metal casing effect to these fluid waves. The tube waves are considered as noise, and they are transversal in the VSP section, where the main interest is to pick the direct downwards and reflected upwards P and S events. Of course, other noise components from the source, medium, sensor, and reception system can be added to the model to explain the data [16].

A central aspect of the VSP technology is filtering for the separation of upgoing and downgoing wave fields, as described in Seeman and Horowicz [31], where a linear stack trajectory can be used for velocity recuperation based on a correlation method like the semblance measure. Data treatment must consider geology as a 3D spatial ambient, where trial-and-error, as well as success, has been accomplished considering 3D-VSP seismic imaging by Li and Hewett [20] based on first arrivals of high registered amplitudes. In a similar technique, Nguyen Dac et al. [25] applied VSP techniques based on primaries and multiples in a marine environment.

Considering a more complex process, Soni and Verschuur [33] applied methods of full wave inversion (FWI) to estimate the subsurface reflectivity, and as a next step, Owusu et al. [28] applied methods of FWI considering an anisotropic model to real data as a 3D-VSP. The physics of reverberation in the borehole fluid has been described by White [38], and mathematically modeled by Mattheij et al. [23].

Alai and Wapenaar [2], among others, summarize the major advantages of VSP survey concerning seismic surface survey and propose to transform surface data into pseudo-VSP data by a numerical wavefield extrapolation using a macro model of the subsurface. This important study represents an improvement to the integration of surface data with real VSP data.

The Negative Gamma Ratio Problem

The present work is justified based on Gregory [14]'s laboratory experiments. Our numerical experiment was designed by including a layer with an anomalous gamma ratio $\left(\gamma = \frac{v_S}{v_P}\right)$ in the seismic model to obtain the VSP sections. Gregory [14] divided rock porosity into classes. For the first class, the velocity behavior does not contradict qualitatively with Frenkel-Biot theory; i.e., the shear wave velocity decreases with the increase of liquid saturation. In the second class, there is a qualitative contradiction with Frenkel-Biot theory; namely, the shear wave velocity increases with the increase of liquid saturation. In the third class, the velocity is pressure-dependent.

The Poisson's ratio (ν) is an important measure in elastic solid mechanics related to pressure prediction, where the γ ratio serving as control quantity. The Poisson's ratio is defined as the negative of the transverse strain rate divided by the axial deformation, expressed as $\nu = -\frac{d\epsilon_{\text{trans}}}{d\epsilon_{\text{axial}}}$. Relating to Lamé's parameters, we have that $\nu = \frac{\lambda}{2(\lambda+\mu)}$. The practical range of values are $-1 < \nu \leqslant 0.5$ [8]. The relationships between Poisson and γ parameters are shown in Fig. 1 and given by the pair:

$$\nu = \frac{1}{2}\frac{(1-2\gamma^2)}{(1-\gamma^2)}, \quad \gamma = \sqrt{\frac{1-2\nu}{2(1-\nu)}}. \tag{1}$$

In Fig. 1 we observe the points of discontinuity and the general behavior of the expressions (1), which are like inverses of each other. These figures intend to show the general mathematical behavior and not laboratory or field experiments. In other words, we open the possibility that field and laboratory measurements may differ and serve as physical bounds.

An important Gregory's [14] lab result is the dynamic experimental detection of abnormal high γ ratios for high porosity rocks. If the γ ratio exceeds $\frac{1}{\sqrt{2}} \approx 0.707$, then we have $\lambda < 0$, and as a result, Poisson's ratio

has a negative value (see Fig. 1). It has long been considered that Poisson's ratio can only assume positive values within the range of 0 to $\frac{1}{2}$. Negative values of Poisson's ratio, in particular, imply that stretching a thin rod by its end faces does not decrease in thickness, but on the contrary, its thickness increases, as a static experiment.

Figure 1: Plot of formulas (1) for the Poisson's and gamma parameters considering a range of theoretical values. Some typical values for the reservoir, source rock, and Poisson's solid values are present in both graphs. The gray and white areas correspond to practical values and purely theoretical values, respectively. Note the discontinuity of the Poisson's ratio, ν(γ), around the value γ=1 (it is not admitted γ<0), the complex discontinuity of the gamma ratio, γ(ν), around the value ν=0.5, and the discontinuity around ν=1. The range 0.5<ν<1 gives the γ ratio a complex value [4].

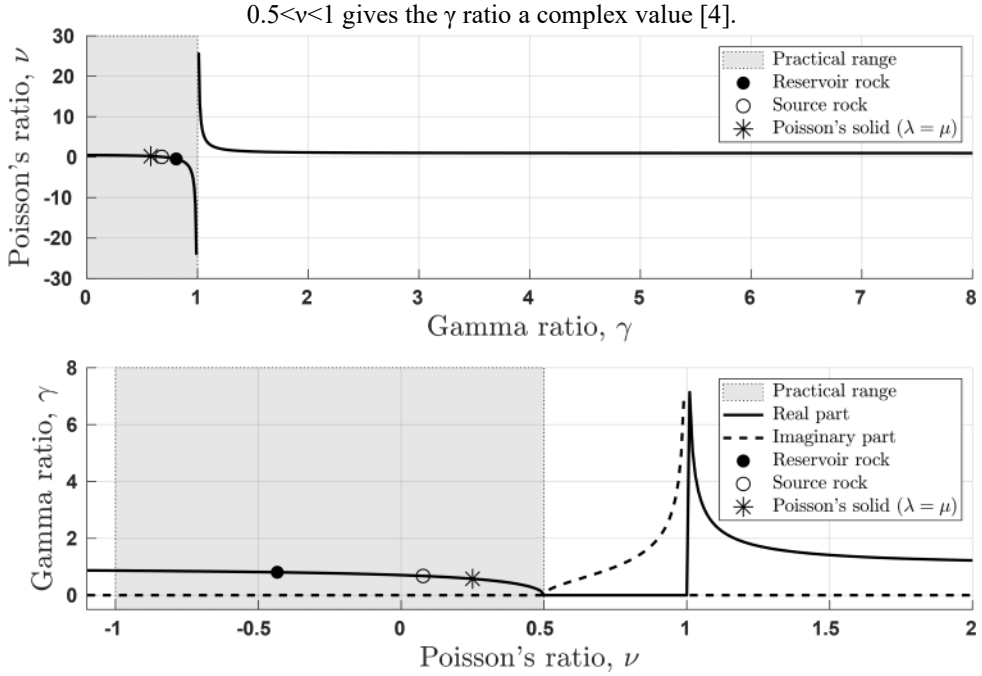

The results of Gregory [14] are not strange, because it does not contradict the fundamentals of thermodynamics about the deformation of a body that demands positive free energy F; i.e., positive values calculated according to the formula

$$\mathrm{F} = \mu\left(\epsilon_{ik} - \frac{1}{3}\delta_{ik}\epsilon_{ll}\right)^2 + \frac{K}{2}\epsilon_{ll}^2. \tag{2}$$

This means that positive values should be for μ and $\mathrm{K} = \lambda + \frac{2}{3}\mu$, but not for λ; hence, Poisson's ratio is not strictly given by positive values [32]. Also, we are dealing with a dynamic measure under wave propagation, and not with a static measure.

The results of Gregory [14] were obtained through dynamic measurements in the laboratory, while other authors, through field experiments, found abnormally high relationships of γ up to 0.77. Static measurements give positive values for the Poisson and gamma ratios. But, there is no complete clearness concerning reasons for such a phenomenon as described by Sibiryakov [32]. For this reason, we assigned the reservoir formation the arbitrarily chosen value $\gamma = 0.816$ to ensure that we can measure the anomaly.

Some questions can be raised as to how sensitive is the estimation of velocities based on the VSP method, taking into account the source pulse, the sampling intervals, the geometry and physical parameters of the model, and the semblance stack operator. To analyze these questions, we tested several different models and parameters and selected for presentation a specific model and semblance correlation techniques using geological information from the sedimentary basins, where exploration for oil and gas is conducted [4].

We constructed testing models with a systematic increase in velocity, but with the intercalation of high- and low-velocity layers, representing geological transgression and regression processes. Sedimentary basin modeling, aiming at oil and gas exploration, contains many theoretical and practical aspects of geology, geochemistry, geophysics, and engineering to characterize the reservoirs, as described by Hantschel and Kauerauf [15] and Ameem [3], among others, which can be included in the model for more practical aspects.

II. Theory

To construct the numerical simulations, the first problem we faced with the VSP method was the interpretation and classification of the events present in the records (useful signal and noise). The second problem was the time-picking process of the event arrivals, where we pointed to the higher amplitudes admitting a minimum phase causal source pulse. Therefore, considering the source pulse, we subtracted the correspondent amount of time Δt to bring the arrival time to a more consistent position. In this process, we considered the pulse with a peak-and-trough form, such that $\Delta t = \frac{1}{4}T_0$ ($f_0 = \frac{1}{T_0}$, the dominant frequency). The vertical and horizontal resolutions should be maintained in the filtering operations in the spectral domain.

The modeling simulated onshore and offshore acquisitions under similar geophysical parameters. The simulated time sections were calculated using the reflectivity method, as is described shortly by Aki and Richards [1], but fully implemented by Sandmeier [30].

The first part of the numerical simulation was surface surveys with onshore and offshore configurations. The source was placed three meters deep, with the explosion represented by a symmetrical pressure field. For a more realistic situation, the records should be affected by local noise, borehole reverberation, the presence of the free surface, and a source pulse of the type that can be more emergent than impulsive. The source pulse had a dominant frequency band, Δf, with a peak frequency $f_p \approx f_0 = 35$ Hz, and a compatible time sampling interval, Δt based on the sampling theorem. The presence of aliasing is more due to the space sampling interval, Δx; therefore, we interpolated traces to have the f − k spectra restricted to the first and second quadrants to better visualize the filtering process.

The VSP simulation used the same basic elastic models for the onshore and offshore cases, where the difference was the water layer on the top of the sequence. The seismic processing of multi-coverage data is based on stack principles, where a functional is optimized for best correlation of the traces along a time trajectory. In a few words, the normalized correlation semblance, $S(v_s; t_0)$, measures the degree of fitting of processed amplitudes, $\overline{u}$, of the traces of a CMP gather for a certain moveout and stack velocity, v_s [5].

Adapted Semblances

For our specific VSP purpose, the conventional functional $S_C(v_s; t_0)$ is adapted as a sum from a first depth $z = z_F$ to a last depth $z = z_L$ (with N_z points), over a temporal window δt (with N_t points) centered at the target reflection time $t_0 = t_0(n\Delta t)$. The functional is explicitly written as:

$$S_C(v_s; t_0) = \frac{\left\{ \frac{1}{N_t} \sum_{t=t_0-\delta t/2}^{t_0+\delta t/2} \frac{1}{N_z} \sum_{z=z_F}^{z_L} \overline{u}[t(z; t_0, v_s)] \right\}^2}{\frac{1}{N_t} \sum_{t=t_0-\delta t/2}^{t_0+\delta t/2} \frac{1}{N_z} \sum_{z=z_F}^{z_L} \{ \overline{u}[t(z; t_0, v_s)] \}^2} \quad (3)$$

.

The measure $S_C(v_s; t_0)$ admits values in the interval [0,1], irrespective of the signal amplitude, and it quantifies the uniformity of the signal polarity throughout the traces. The quantity $S_C(v_s; t_0)$ is proportional to the energy ratio between the numerator and denominator of equation (3). The resulting moveout corrected section represents the validity of the event picking process, and this coherence measure showed to be very effective in our experiments, which we classify as manual picking.

Another semblance coherence measure used was the complex semblance, which can be followed in Bernabini et al. [5]. In this case, we have a complex continuous function ψ expressed by:

$$\psi(z, t) = \overline{u}(z, t) + \mathbf{i}\, q(z, t); \quad (4)$$

where $q(z, t)$ is obtained from $\overline{u}(z, t)$ by applying the Hilbert transform, $\mathbf{H_t}$, to the traces (with respect to the independent variable t), i.e.,

$$q(z, t) = \mathbf{H_t}\{\overline{u}(z, t)\}, \quad (5)$$

therefore, we deal with an analytical signal, where the amplitudes are taken from the trace envelope instead of directly from $\overline{u}(z, t)$. The complex semblance, S_X, is defined as:

$$S_X(v, t_0) = \frac{\sum_{t=t_0-\delta t/2}^{t_0+\delta t/2} \left| \frac{1}{N_z} \sum_{z=z_1}^{z_2} \psi(z, t; v) \right|^2}{\sum_{t=t_0-\delta t/2}^{t_0+\delta t/2} \frac{1}{N_z} \sum_{z=z_1}^{z_2} |\psi(z, t; v)|^2} \quad (6)$$

where the vertical bars denote the modulus of the complex number; hence the value of $S_X(v, t_0)$ is real. This coherence measure was shown to be effective in our experiments, and complementary to the conventional semblance, $S_C(v, t_0)$.

The so-called AB-semblance, as described by Fomel [11], was also implemented and analyzed together with the conventional and complex semblance measures. However, only the solutions given by the conventional and complex semblance measures were consistent enough and chosen for demonstration.

Time Trajectories

For the VSP numerical experiments, the NMO correction used the velocity values, v_{nmo}, from the optimization of the $S(v_{\text{nmo}}; t_0)$ functional along a specific linear trajectory $t(z; t_0, v_{\text{nmo}})$ given by:

$$t(z; t_0, v_{\text{nmo}}) = t_0 + \frac{z - z_0}{v_{\text{nmo}}}. \tag{7}$$

That is, we define a linear trajectory to describe the up-going field reflected from the bottom (at depth z_0) of the target zone. In another optimization process for reference, we implemented an automatic search for the estimation of the parameter v_{nmo} in the semblance domain, as described by Leite e Vieira [19], which can be used in a future numerical experiment.

For comparison reasons, time trajectories in surface seismic reflection, the NMO correction and stack, based on the function $S(v_{\text{s}}; t_0)$, gives the optimum value of v_{s} in $S(x; t_0, v_{\text{s}})$ for the hyperbolic trajectory:

$$t(x; t_0, v_{\text{s}}) = \sqrt{t_0^2 + \frac{x^2}{v_{\text{s}}^2}}, \tag{8}$$

which is the conventional hyperbolic trajectory. Other $t(x; t_0, m)$ trajectories are given for different stack methods as the CRS described by Mann [22], with a specific hyperbolic trajectory given by:

$$t(x_m, h; t_0, \mathbf{m}) = \sqrt{\left[t_0 + 2\frac{\sin(\alpha_0)}{v_0}(x_m - x_0)\right]^2 + 2t_0\frac{\cos^2(\alpha_0)}{v_0}\left[\frac{(x_m - x_0)^2}{R_{\text{N}}} + \frac{h^2}{R_{\text{NIP}}}\right]}, \tag{9}$$

where $\mathbf{m} = (\alpha_0, R_{\text{N}}, R_{\text{NIP}})$ is the parameter vector of the wave field attributes which are determined in the optimization process. The CRS stack method was applied by Von Steht [35] and Goertz [37] by tracing different paraxial ray trajectories, and Von Steht [36] looking at real VSP data problems.

The Tubes Waves

The phenomenon of hydraulic tube waves is rather complex for modeling but well-registered. The phenomenon is related to the borehole shape and construction, water content, mud properties, casing, cables, pressure stage around the borehole, microearthquakes, dispersion, resonance, soft and hard formations, multiples, and frequency band of the power source. The physical mechanism of tube waves called attention and research interest [13]. This complexity signalizes that the survey should be conducted in a depth interval involving the desired target, which is translated in the VSP time-depth section as a rectangle with the corners (t_1, z_1), (t_2, z_1), (t_1, z_2) and (t_2, z_2).

Hydraulic compressional waves (HW) propagate with high amplitude along the cylindrical column filled with fluid and represent the major source of systematic noise in the VSP recorded data. The velocity for the uncased borehole is given by:

$$v = v_0\sqrt{\frac{\mu}{\mu + K_0}}, \tag{10}$$

where μ is the shear module of the borehole rock, v_0 is the velocity of the fluid (mud filling) contained in the borehole, and K_0 is the bulk modulus of the mud material. Typical values of these parameters are described by Carcione and Poletto [7].

The presence of the metal casing makes the velocity of the HW to increase, which is then expressed by:

$$v = v_0\sqrt{1 + \frac{K_0 D}{Ed}}, \tag{11}$$

where D and d are, respectively, the diameter and the thickness of the casing, and E is the Young modulus of the casing metal. The physics of this process is described, for instance, by Noris [26].

Modeling by the Reflectivity Method

The construction of a numerical experimental model can have many options, and an obvious selection is one as close as possible to a real geological case. We follow here the line of thought of Steeghs and

Drijkoningen [34] that clearly satisfies our present 1D forward modeling. The experimental models were designed with a velocity gradient, periodic and random distribution of parameters, and mixed patterns; besides, we focused at a depth interval and velocity. Therefore, the velocity-depth model has been divided into three parts: the top (considered statistically known), the target interval, and the bottom which can produce some events as noise.

The full wave displacement field modeling used is known as the *reflectivity method*, and its description can be followed in Fertig and Muller [10], Aki and Richards **Error! Reference source not found.**, Muller [24], and Ma et al. [21], among others. The reflectivity method includes the effects of geometrical spreading and conversions between P and S waves. It simulates seismic sections along surface profiling or depth in the borehole. Its limitations for treating real data from complex geology can be recognized directly from the model shown in Fig. 15, formed by plane, homogeneous, isotropic layers. This model is usual in stack and migrations processes; the postulate is that this geometry serves to treat data in a small source-sensor aperture.

The problem solved by the reflectivity method is the integration of the elastodynamic equation given by:

$$(\lambda + 2\mu)\nabla(\nabla \cdot \mathbf{u}) - \mu\nabla \times (\nabla \times \mathbf{u}) - \rho\ddot{\mathbf{u}} = \mathbf{f}, \tag{12}$$

for the displacement vector $\mathbf{u} = (t, u_x, u_y, u_z)$, under the geometry and boundary conditions described with the multilayer model of Fig. 15, which allows for a convenient separation of the displacement components. Using the radial symmetry in the cylindrical coordinates, the solution for the 3D spectral components (U_z, U_r, U_ϕ) is expressed by:

$$U_z(r, z \mid \omega) = \frac{1}{2\pi} \sum_{m=-\infty}^{\infty} \int_0^{\infty} u_z^0(k, m, z, \omega)\omega^2 p J_m(\omega pr) d(pr), \tag{13}$$

$$U_r(r, z \mid \omega) = \frac{1}{2\pi} \sum_{m=-\infty}^{\infty} \int_0^{\infty} u_r^0(k, m, z, \omega)\omega^2 p \frac{d}{d(\omega pr)} J_m(\omega pr) d(pr), \tag{14}$$

$$U_\phi(r, z \mid \omega) = \frac{1}{2\pi} \sum_{m=-\infty}^{\infty} \int_0^{\infty} u_\phi^0(k, m, z, \omega) \frac{1}{r^2}\omega^2 \frac{d}{d(\omega pr)} J_m(\omega pr) d(pr), \tag{15}$$

where u_z^0, u_r^0 and u_ϕ^0 are the propagation reflection-transmissions coefficients. The computation is performed for a large ω frequency band, and the inverse Fourier transform gives the time response considering the traces as real functions. The Green's function, G_{ij}, for the problem is a tensor in cylindrical coordinates, $G_{ij}, (i, j = r, \phi, z)$, with the radial, r, transversal, ϕ, and vertical, z, components.

III. Numerical Results

VSP Configuration and Sequence of Results

The specific VSP configuration used is named VSP-SO (single offset). For the numerical experiments, the chosen source positions were 100, 300, and 600 meters away from the top of the borehole and measured along the surface. The borehole is considered vertical; therefore, the trajectories (primaries and multiples) are close to the vertical with a small incidence angle; for large angles, the possible effects are analyzed by **Error! Reference source not found.** in the AB semblance method, where the P-SV-SH spreading across the interfaces are taken into consideration.

The different experiments had in general 512 points, 60 sensors distributed around the target layer, and variable offsets producing tables and figures. The models were constructed under the following geological criteria:

1. Transgressive and regressive periodical phenomena;
2. Random distribution of parameters;
3. General increasing velocities with depth;
4. General increasing velocities with depth, and random distribution of parameters;
5. Presence of anomalous Poisson ratio in the target layer.

The figures for analysis of the computational results follow an order that reflects the algorithm's sequence:

1. Distributions for P and S velocities and density in the layered medium;
2. VSP sections for u_z, u_r, u_ϕ, and their aliased spectrum;

3. Interpolated VSP sections (u_z, u_r, u_ϕ) and their non-aliased spectrum;
4. Filtered spectral sections (for u_z, u_r, u_ϕ) to obtain the desired ascending field;
5. Inverse Fourier transform to obtain u_z, u_r, u_ϕ VSP sections;
6. Interpretation of VSP sections by simple straight ray tracing;
7. Calculation of the semblance maps and their interpretation;
8. NMO correction based on the interpretation of the semblance map;
9. Table of P and S velocities estimation and the gamma ratio for the target zone and surroundings.

Geometrical and Physical Model

Figure 2 shows a complex geological input model used in the computational experiments, and chosen for display. The model is formed by six (6) layers over a half-space, where the necessary parameters for the simulation can be seen. The parameters used are also displayed in Table 1. The results for u_z, u_r, and u_ϕ, with the correspondent figures, are limited by the number of pages for the article. Other numerical results can be found in [9].

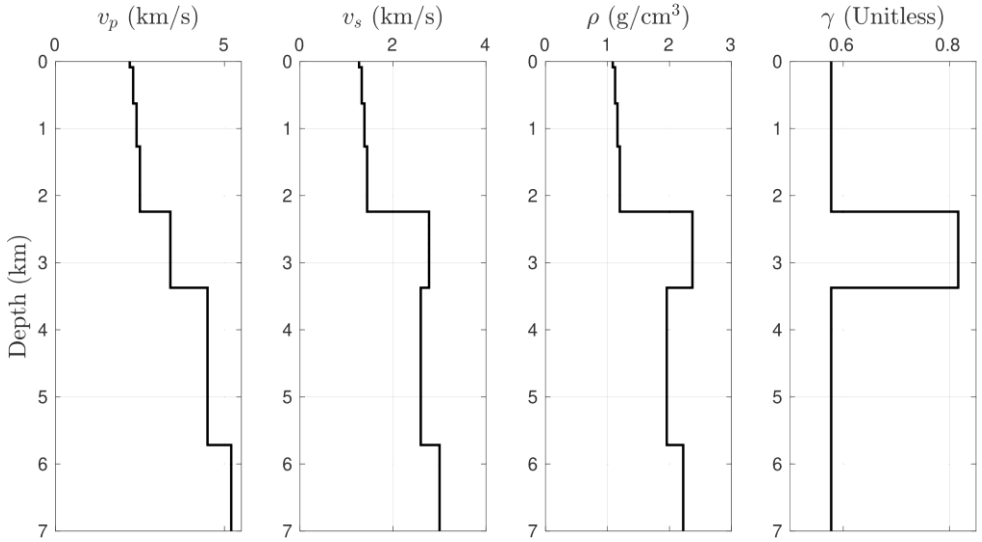

Figure 1: Model named 6-layers over a half-space. The target is the layer number 5 (see Table 1).

Table 1: Layer number, thickness, P and S velocities, density, and the γ ratio for the 6-layer model over a half-space. The fifth layer has an anomalous γ value, the goal for discrimination in the semblance domain, and is the target layer.

Layer	Thickness (m)	$v_p(km/s)$	$v_s(km/s)$	$\rho(g/cm^3)$	γ
1	87	2.200	1.2702	1.0854	0.577
2	540	2.300	1.3279	1.1232	0.577
3	641	2.400	1.3857	1.1611	0.577
4	972	2.500	1.4434	1.1990	0.577
5	1133	3.400	2.7760	2.3710	0.816
6	2344	4.500	2.5982	1.9566	0.577
Half-space	$+\infty$	5.200	3.0023	2.2218	0.577

Time Sections: Vertical, Transversal, and Radial Components

P-wave picking is normally done in the vertical component, but the radial component can also be used for this purpose. Similarly, the SH-wave picking is normally done in the transversal component, but the radial component can also give such information regarding the SV-wave. The picking process depends on the intrinsic angle of reflectivity (and the P-SV-SH spreading according to Snell's law) from the bottom of the target zone (layer).

Figures 3, 4, and 5 are, respectively, the vertical, transversal, and radial components representing the time section for systematic analysis, and constructed with the reflectivity method; their input model is shown in the Fig. 2. For processing the time sections, we first performed trace interpolation along the depth axis for the spectrum to have the least aliasing along the f_z frequency axis; i.e., we constrained the information to the first and second spectral quadrants. Also, to be more realistic, a 5% (of the maximum amplitude) random noise level was added systematically to the reflectivity output. A full interpolated section can blur the figure.

The major part of the process is the filtering to separate the up and down events. This part showed that one needs forward modeling, experience, and try-and-error practice. In figures 3, 4, and 5 we can observe the events that correspond to the direct wave, the tubular wave, and reflection, where the discriminant is the velocity (event's inclination in the time section with a convenient scale). In the filtered time section (ascending field), the time of the direct wave increases linearly, while for the desired reflection event the time decreases linearly.

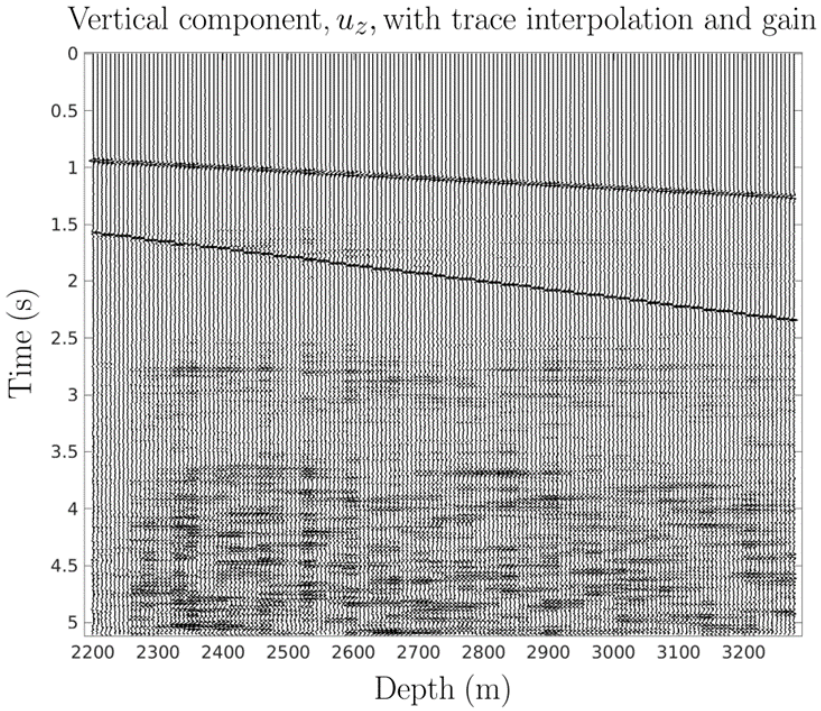

Figure 2: Vertical component, u_z, of the VSP time section, P-SV field, with trace interpolation along the z axis, additive noise, and gain. The events are interpreted as the direct waves, tubular waves, and reflections. For the direct waves, the time increases linearly with depth. For the weak target bottom reflections, the time decreases linearly with depth.

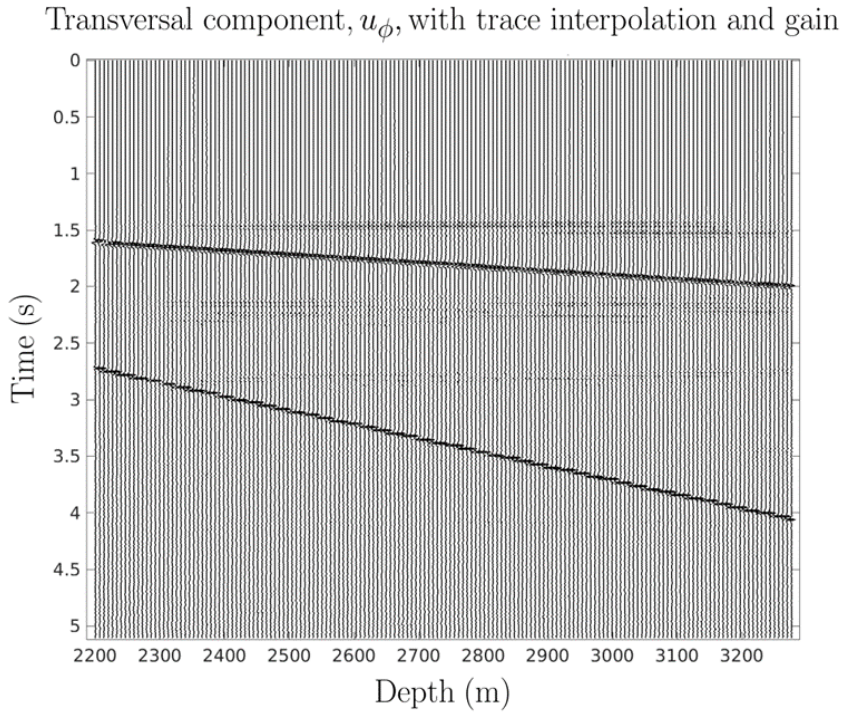

Figure 3: Transversal component, u_ϕ, of the VSP time section, SH field, with trace interpolation along the z axis, time gain, and additive noise. The events are interpreted as the direct waves, tubular waves, and reflections. For the direct wave, the time increases linearly with depth. For the weak target bottom reflection, the time decreases linearly with depth.

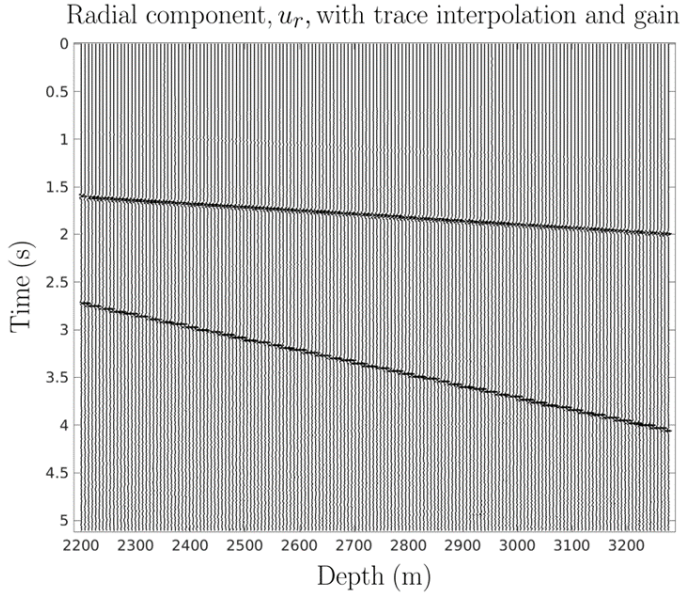

Figure 4: Radial component, u_r, of the VSP section, P-SV field, with trace interpolation along the z axis, time gain, and additive noise. The present events are interpreted as direct waves, tube waves, and reflections. For the direct waves, the time increases linearly with depth. For the weak target bottom reflections, the time decreases linearly with depth.

Filtering Sections: Vertical, Transversal, and Radial Components

Figures 6, 7, and 8 show the sequence of $f - k$ spectra of Fig. 3, 4, and 5, respectively, and the applied ideal band-pass velocity filter. On the top of each figure, we have the original spectrum showing the strong aliasing; in the middle, the trace interpolated spectrum showing the constraint spectrum to the first and second quadrants; on the bottom, the band-pass filtered desired event. The desired event is placed in the second quadrant and slightly dipping left. This sequence of figures represents an important part of our research efforts because the up and down fields must be separated before the velocity estimation be performed. From the bottom

figures, we can see that the 2D band-pass filter has the property of an ideal (sharp cut-off) band-pass filter; smooth edge filters should be tested for resolution. After the application of the filter, the inverse Fourier transform is performed to obtain the VSP seismic section back for further processing, and coherence semblance velocity analysis for P and S waves.

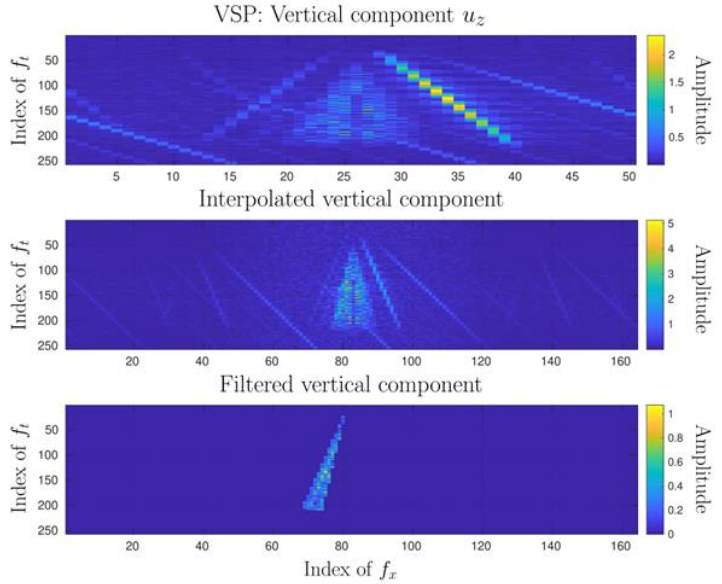

Figure 5: Stages of the $f - k$ band-pass filtering of Fig. 3. (Top) original (not interpolated) amplitude spectrum, first and second quadrants. (Middle) the spectrum of the section with interpolated traces along the z axis to increase the space Nyquist frequency. (Bottom) ideal band-pass velocity filter applied.

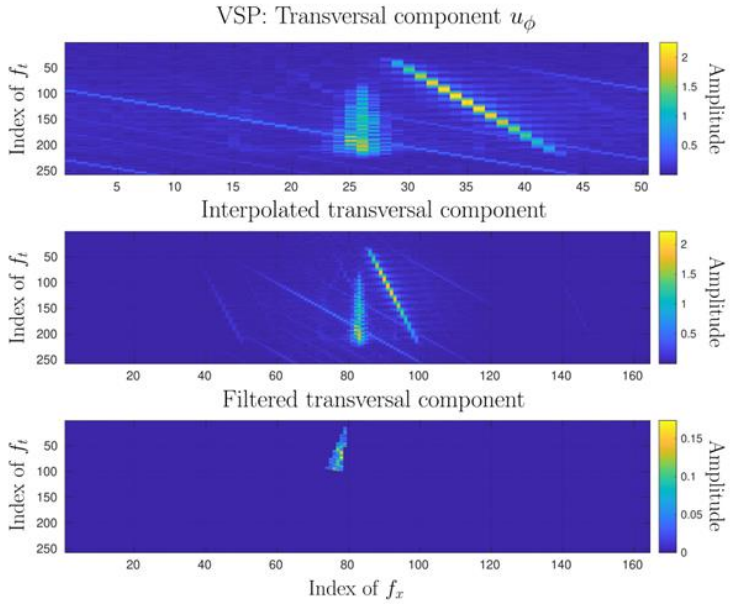

Figure 6: Stages of the f – k band-pass filtering of Fig. 4. (Top) the original (not interpolated) amplitude spectrum, first, and second quadrants. (Middle) the spectrum of the section with the interpolated traces along the z axis to increase the space Nyquist frequency. (Bottom) the ideal band-pass velocity filter applied.

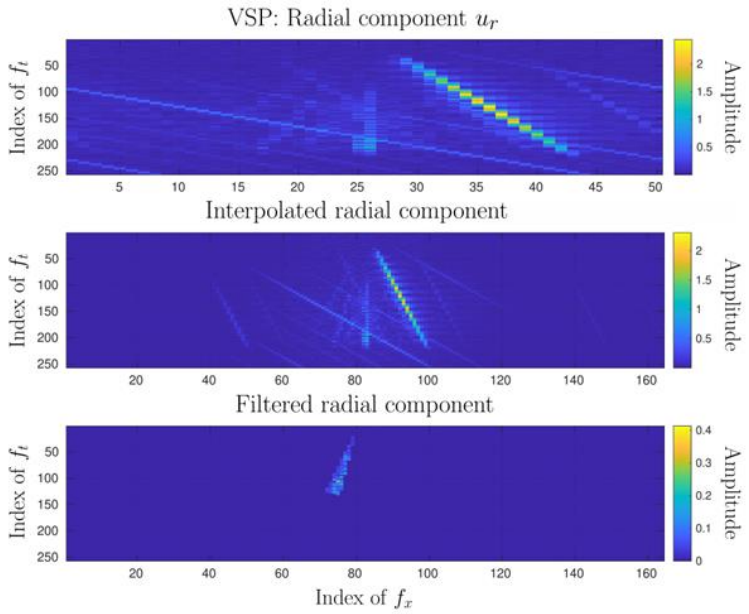

Figure 7: Stages of the f – k band-pass filtering of Fig. 5. (Top) the original (not interpolated) amplitude spectrum, first, and second quadrants. (Middle) the spectrum of the section with the interpolated traces along the z axis to increase the space Nyquist frequency. (Bottom) the ideal band-pass velocity filter applied.

Semblance Sections: Vertical, Transversal, and Radial Components

Figures 9, 10, and 11 show on the left the inverse Fourier transform of the entire section from the band-pass filtered data of figures 6 (bottom), 7 (bottom), and 8 (bottom), respectively, where the shown main events are the desired reflection from the bottom of the target zone. On the right side of figures 9, 10, and 11, we have the output of the semblance algorithm showing the coherent high concentration of the desired P- and S-wave primary events. From the interpreted conventional semblance map, the arrow-pointed events give a sharp velocity picking summarized in Table 2 for the 3D sensors positioned in the target layer, as shown in Fig. 2, and given in Table 1. The three-digit decimal values are given by the picking on the computer monitor.

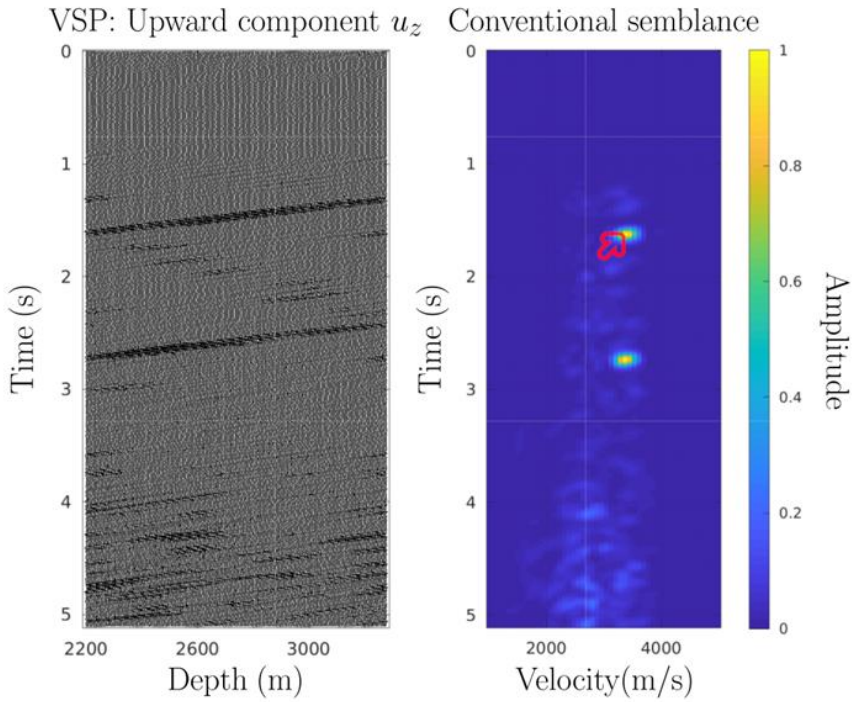

Figure 8: Upward field and semblance map. (Left) inverse Fourier transform of the band-pass filtered data of Fig. 6 (bottom), which corresponds to the vertical component, u_z, of the upward reflection field from the bottom

of the target zone. (Right) the conventional semblance map that corresponds to the coherence measure for the left section along linear trajectories. The arrow points to the P-wave at 1.616 s and a $v_{nmo} = 3425$ m/s. At 2.70 s there is a multiple with the same velocity of 3425 m/s.

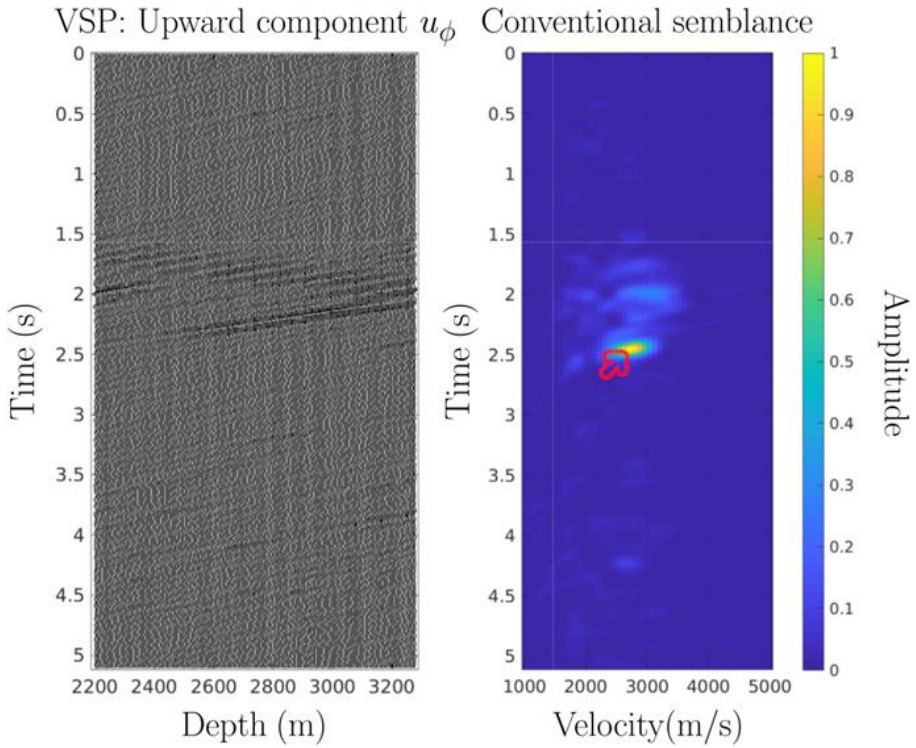

Figure 9: Upward field and semblance map. (Left) inverse Fourier transform of the band-pass filter data of Fig. 7 (bottom), which corresponds to the transversal component, u_ϕ, of the upward reflection field from the bottom of the target zone. (Right) the conventional semblance map that corresponds to the coherence measure for the left section along linear trajectories. The arrow points to the SH-wave at 2.458 s and a $v_{nmo} = 2778$ m/s. The multiples are present but relatively weak in this plot.

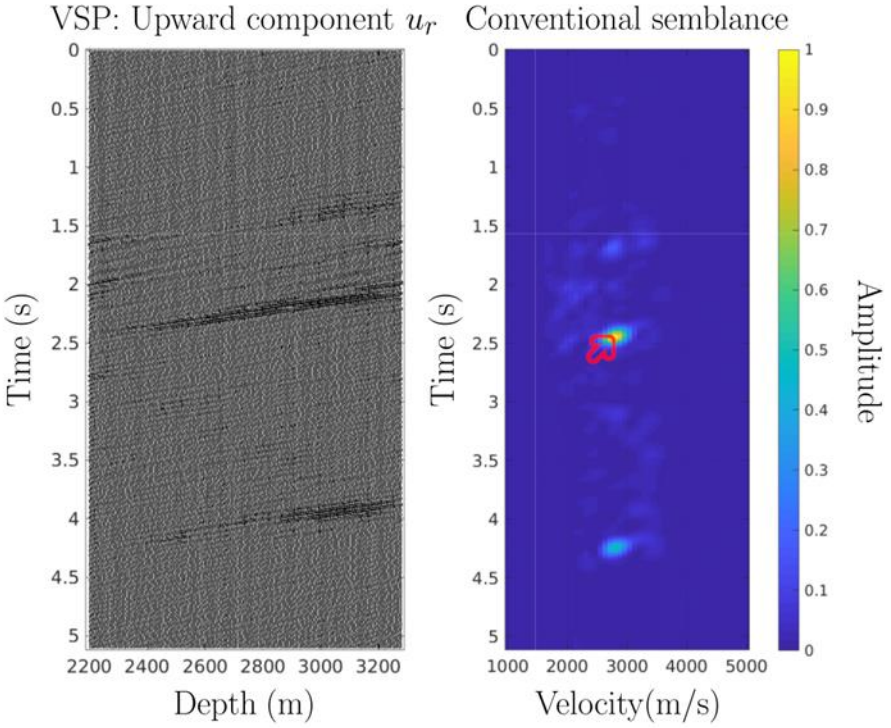

Figure 10: Upward field and semblance map. (Left) inverse Fourier transform of the band-pass filter data of Fig. 8 (bottom), which corresponds to the radial component, u_r, of the upward reflection field from the bottom

of the target zone. (Right) the conventional semblance map that corresponds to the coherence measure for the left section along linear trajectories. The arrow points to the SV-wave at 2.439 s and a $v_{nmo} = 2736$ m/s. At 4.26 s there is a multiple with the same velocity of $v_{nmo} = 2736$ m/s.

Stages of VSP Sections: Vertical, Transversal, and Radial Components

Figures 12, 13, and 14 summarize the three stages of the VSP field separation for qualitative analysis. Starting left, the original interpolated time section; in the middle, the upward seismic field component; and on the right, the NMO corrected upward field after the semblance velocity picking. The NMO section is the strong validation technique for the semblance velocity-picking process in the present study.

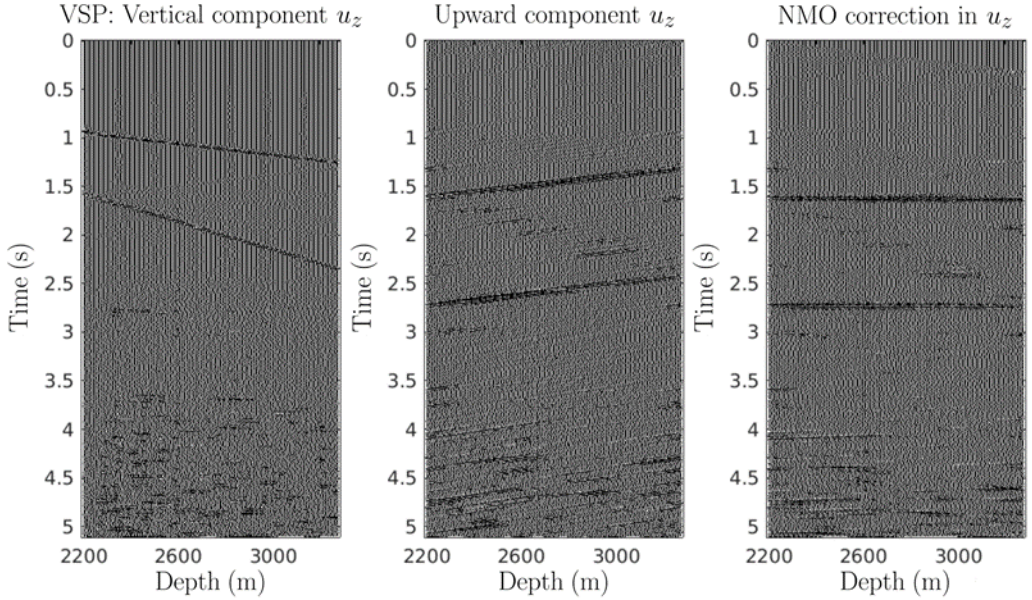

Figure 11: Stages of the VSP processing, P-SV field. (Left) original interpolated time section. (Middle) upwards filtered component. (Right) NMO corrected time section showing the expected flattened event from the semblance velocity picking around 1.616 s for the P wave with $v_{nmo} = 3425$ m/s. At $t = 2.70$ s there is a multiple arrival with the velocity of the P wave.

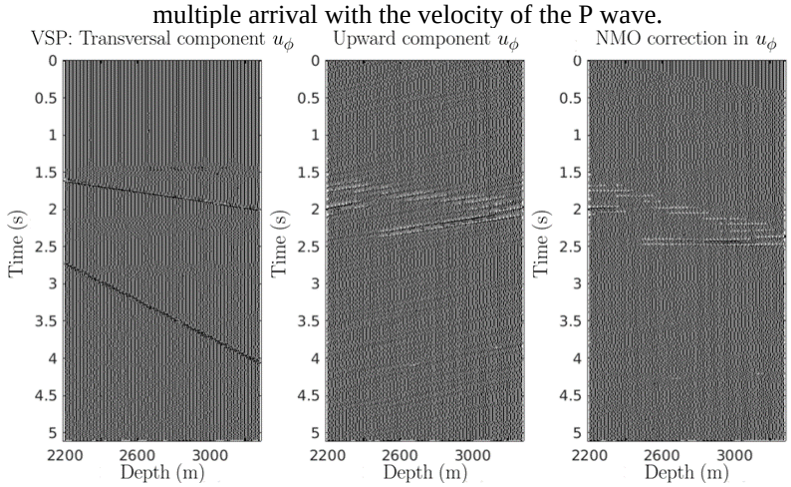

Figure 12: Stages of the VSP processing, SH field. (Left) original interpolated time section. (Middle) upwards filtered component. (Right) NMO corrected time section showing the expected flattened event from the good semblance velocity picking at 2.458 s for the SH wave with velocity $v_{nmo} = 2778$ m/s. Early internal arrivals and multiples are placed above the focus event.

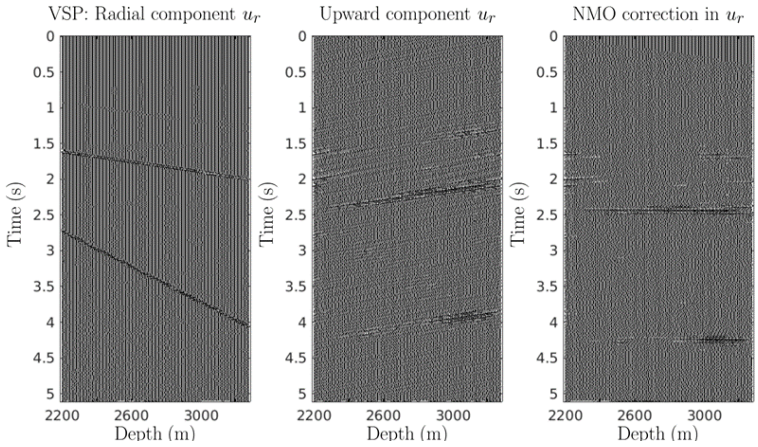

Figure 13: Stages of the VSP processing, P-SV field. (Left) original interpolated time section. (Middle) upwards filtered component. (Right) NMO corrected time section showing the expected flattened event from the good semblance velocity picking around 1.616 s for the P wave with velocity $\mathrm{v_{nmo}} = 3425$ m/s, and at 2.439 s for the SV wave with velocity $\mathrm{v_{nmo}} = 2736$ m/s.

Results Summary Table

Table 2 summarizes the velocity picking process in the semblance domain for the three seismic u_z, u_r, and u_ϕ components. The P-wave was easily picked from the u_z component, and the SH-wave from the u_ϕ component. In the numerical experiment, the u_r component allowed also for picking the SV-wave mode, as a double check. The P-SV-SH spreading is expected to be an important issue in this modeling for different normal incidence angles. The figures shown are only for a set of values when the sensors are positioned in the target layer, otherwise, too many figures would have to be shown in this paper.

Table 2: Example of the picked time, t_0, and velocities, v_{nmo}, for the anomalous layer in the correspondent semblance map, S-conventional and S-complex, and the u_z, u_ϕ and u_r sections. The 3D sensors are positioned in the target layer of the 6-layer model, as can be seen in Fig. 2. We did not show similar table for the layers above and below the target layer to spare space.

P-wave, component: $u_z(t_0, v)$			
t_0 (s)	S_C-conventional: v	t_0	S_X-complex: v
1.616	3425	1.616	3448
SH-wave, component: $u_\phi(t_0, v)$			
t_0 (s)	S_C-conventional: v	t_0	S_X-complex: v
2.458	2778	2.458	2724
SV-wave, component: $u_r(t_0, v)$			
t_0 (s)	S_C-conventional: v	t_0	S_X-complex: v
2.400	2736	2.439	2805

For the sensors positioned in the layer above the target layer, the calculation of the gamma ratio from the conventional and complex semblance maps gives the following results:

$$\gamma = \frac{v_s}{v_p} = \frac{1448}{2517} = 0.575, \quad \text{where} \quad \Delta\gamma = 0.35\%, \tag{16}$$

$$\gamma = \frac{v_s}{v_p} = \frac{1448}{2494} = 0.580, \quad \text{where} \quad \Delta\gamma = -0.51\%. \tag{17}$$

For this experiment, the deviation $\Delta\gamma$ from the real values is smaller for the conventional semblance. The real values are in Table 1.

For the sensors positioned in the target layer, the calculation of the γ ratios from the conventional and complex semblance maps gives the following results:

$$\gamma = \frac{v_\mathrm{S}}{v_\mathrm{P}} = \frac{2778}{3425} = 0.811, \quad \text{where} \quad \Delta\gamma = 0.61\%, \tag{18}$$

$$\gamma = \frac{v_\mathrm{S}}{v_\mathrm{P}} = \frac{2724}{3448} = 0.790, \quad \text{where} \quad \Delta\gamma = 3.18\%, \tag{19}$$

which shows a rather good agreement measured by the deviation in percentage, concerning Table 1.

For the sensors positioned in the layer below the target layer, the calculation of the gamma ratios from the conventional and complex semblance maps gives the following results:

$$\gamma = \frac{v_s}{v_p} = \frac{2425}{4184} = 0.579, \quad \text{where} \quad \Delta\gamma = -0.34\%, \tag{20}$$

$$\gamma = \frac{v_s}{v_p} = \frac{2437}{4230} = 0.576, \quad \text{where} \quad \Delta\gamma = 0.17\%. \tag{21}$$

For this model, the deviation $\Delta\gamma$ is smaller for the complex semblance. The real values are in Table 1

IV. Conclusions

Our main conclusions are related to the initially established goals to look at how sensitive is the gamma ratio, $\gamma = \frac{v_S}{s_P}$, estimation in a layered medium with variation of velocity, principally around an anomalous γ ratio. The theory says that a geological reservoir can be characterized by an anomalous high γ ratio surrounded by normal γ (values around the Poisson's solid, with physical Lamé's parameters $\mu \approx \lambda$). The results are displayed over the $t - z$ seismic sections and geological images are simply interpreted.

The first point to highlight is the necessity of full control of the geology converted to a geophysical model expressed by geometry and physical parameters. The second is to properly describe the target zone for investigation. The third is the band-pass filtering process to separate the upward from the downward field propagation components. The fourth is the importance of having a non-aliased spectrum that can be obtained by interpolation. The fifth is the full control of the semblance method for picking events which should be described by a specific time trajectory that will be dependent on the source-sensor offset.

The results obtained in the experiments for the measure of the γ ratio showed a relatively small error less than 5%, concerning the real value, which we consider a good numerical result. The effect of higher noise in the data is to smear off the velocity picking in the semblance domain.

A further investigation should be done to compare the reflectivity method with the classical ray theory on the same model. It is clear that ray tracing takes better care of complex geological cases due to lateral variations, like the presence of domes, but it needs more explicit parameter control. Naturally, the application to real 3C data is certainly the next step up to examine the possibility of anomalous γ ratios, in a strategic picking procedure, as in the case of velocity analysis and stack followed by migration.

Acknowledgements

The authors would first like to thank the reviewers for their patience and positive contributions. We would like to thank the Brazilian institutions UFPA (*Universidade Federal do Pará*), and the project National Institute of Science and Technology (*Instituto Nacional de Ciência e Tecnologia, INCT-GP, of MCT/CNPq/FINEP*) for the research support aiming at oil and gas exploration. Our thanks are also extended to CNPq for the scholarship.

Short Resume of The Reflectivity Method

The forward modeling used the reflectivity method as described by Aki and Richards [1], implemented by Sandmeier [30], and shortly discussed by Ma et al. [21], among other authors. The reflectivity method is mostly used to simulate body waves, and it includes geometrical spreading, conversions P-SV-SH, and simulates seismic sections along a surface profiling, $x - y$, or along the depth, z. The limitations for analyzing real data from complex geology can be recognized directly from the geometrical model of Fig. 15, which is formed by plane, homogeneous, and isotropic layers. However, this model is usual in stack and migration processing. The postulate is that this geometry serves to treat data in a small source-sensor aperture.

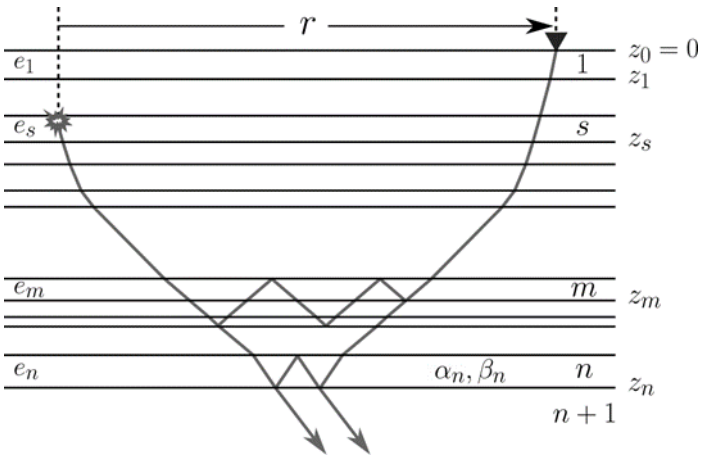

Figure 14: The geometry and parameter distribution in the reflectivity model, following Aki and Richards [1].

The basic idea of the reflectivity method is to decompose the solution of the non-homogeneous elastodynamic equation:

$$\rho\ddot{\mathbf{u}} = \mathbf{f} + (\lambda + 2\mu)\nabla(\nabla \cdot \mathbf{u}) - \mu\nabla \times (\nabla \times \mathbf{u}), \tag{22}$$

in terms of vertical and horizontal propagation. Therefore, the model is represented by vertically stratified earth, where $\mathbf{u} = (t, u_x, u_y, u_z)$ is the temporal displacement vector, $\mathbf{u} = \mathbf{u}(t, \mathbf{x})$, $\ddot{\mathbf{u}}$ the second order time derivative, ρ the density of the layer with λ and μ its Lamé's parameters, ∇ the vector operator for the field gradient, divergence and curl. The vector $\mathbf{f} = \mathbf{f_I}$ plays the role of the internal body forces (gravity and magnetic between internal particles), that is considered null; this condition makes the system (22) homogeneous. Then, $\mathbf{f}$ takes another format as the external source function distributed in time and space, $\mathbf{f} = \mathbf{f_E}$, and the system (22) becomes inhomogeneous; therefore, we expect a convolution between the source function and the medium impulse response.

Equation (22) is submitted to the Lamé-Helmholtz decomposition theorem for the source vector function $\mathbf{f}$, and displacement vector $\mathbf{u}$, in terms of displacement potentials (ϕ scalar and $\boldsymbol{\Theta}$ vectorial) as described by Saada [29]. The decomposition is:

$$\mathbf{u} = \nabla\phi + \nabla \times \boldsymbol{\Theta}, \quad \nabla \cdot \boldsymbol{\Theta} = 0, \tag{23}$$

$$\mathbf{f} = \nabla\Phi + \nabla \times \boldsymbol{\Psi}, \quad \nabla \cdot \boldsymbol{\Psi} = 0. \tag{24}$$

The vector potential $\boldsymbol{\Theta}$ in (23) represents the S-wave, and is further decomposed into two scalar potentials, ψ for the SV component, and χ for the SH component, then we have that:

$$\mathbf{u} = \nabla\phi + \nabla \times \nabla(0,0,\psi) + \nabla \times (0,0,\chi). \tag{25}$$

The source vector term (considering only the external contribution, $\mathbf{f} = \mathbf{f_E}$) is similarly expressed with Greek capital letters by:

$$\mathbf{f} = \nabla\Phi + \nabla \times \nabla(0,0,\Psi) + \nabla \times (0,0,X). \tag{26}$$

The result of the algebraic is the set of equations of motion for the P, SV, and SH-waves, in terms of displacement potentials, as given by:

$$\alpha^2\nabla^2\phi - \ddot{\phi} = -\frac{\Phi}{\rho}, \quad \beta^2\nabla^2\psi - \ddot{\psi} = -\frac{\Psi}{\rho}, \quad \beta^2\nabla^2\chi - \ddot{\chi} = -\frac{X}{\rho}, \tag{27}$$

where $\alpha^2 = \frac{\lambda+2\mu}{\rho}$, $\beta^2 = \frac{\mu}{\rho}$; $\alpha = v_{\mathrm{P}}$, and $\beta = v_{\mathrm{S}}$.

This summary exposes the propagation of the potentials in terms of the wave equations in the form ((27)); besides, this independent propagation is valid for one layer with constant physical parameters (α, β, λ, and ρ). The transmission of energy between sequential layers is set by the boundary conditions. The non-homogeneous partial differential equations (27) is solved in circular-cylindrical coordinates (radial, azimuthal, depth), to account for the horizontal symmetrical (lateral) propagation, allowing the heterogeneity of the model to the vertical axis (z).

The solution to equation (25) is obtained by the method of separation of variables, and Fourier transformation from time to frequency. Then, the superposition of basic infinite Fourier components is written in the general form:

$$f(\omega) = \int_{-\infty}^{\infty} f(t)e^{+i\omega t}, \quad f(t) = \frac{1}{2\pi}\int_{-\infty}^{\infty} f(\omega)e^{-i\omega t}, \quad \text{(time)}, \tag{28}$$

$$f(k) = \int_{-\infty}^{\infty} f(x)e^{-ikx}, \quad f(x) = \frac{1}{2\pi}\int_{-\infty}^{\infty} f(k)e^{+ikx}, \quad \text{(space)}. \tag{29}$$

Vertical and Horizontal Propagations

The solution for the displacement potentials in circular-cylindrical coordinates is:

$$\phi(\mathbf{x},\omega) = J_m(kr)e^{im\phi}(Ae^{-\gamma z} + Be^{\gamma z})e^{-i\omega t},$$

(30)

$$\psi(\mathbf{x},\omega) = J_m(kr)e^{im\phi}(Ce^{-\nu z} + Be^{\nu z})e^{-i\omega t},$$

(31)

$$\chi(\mathbf{x},\omega) = J_m(kr)e^{im\phi}(Ee^{-\nu z} + Fe^{\nu z})e^{+i\omega t}.$$

(32)

where A, B, C, D, E, and F are the integration constants, m is an integer, $J_m(kr)$ the mth-order Bessel function, $\gamma = (k^2 - \omega^2/\alpha^2)^{1/2}$, $\nu = (k^2 - \omega^2/\beta^2)^{1/2}$.

With the above potential constructions, the propagation is separated into two parts: the horizontal, (r,ϕ), and the vertical (z) components. The horizontal propagation is expressed by the term $Y_k^m(r,\phi) = J_m(kr)e^{im\phi}$. The vertical component is represented in the exponential terms $e^{\pm\gamma z}$ and $e^{\pm\nu z}$, where the layer strata are represented by the physical parameters, and by the geometry (layer thickness and depth).

In the $f-k$ spectral domain, the vertical propagation is summarized in terms of plane waves as a matrix differential equation in the form:

$$\frac{\partial \mathbf{f}}{\partial z} = \mathbf{A}\mathbf{f},$$

(33)

where **A** is a constant square matrix composed of elastic parameters of a particular layer, and **f** is a column matrix for particle displacement and stress starting at the source level. Therefore, the construction of the matrices **A** and **f** start from the equation of motion in the stress form for the basic SH and P-SV, as given by:

$$\rho\ddot{u}_i = \tau_{ij,j} + f_i.$$

(34)

Equation (34) allows the construction of the propagation in terms of a matrix product from depth z_n to z_m, and boundary conditions, as:

$$\mathbf{f}(z_m) = \mathbf{P}(z_m, z_n)\mathbf{f}(z_n),$$

(35)

where the propagator matrix $\mathbf{P}(z_m, z_n)$ is known explicitly and carries the information through the layering, and **f** the amplitudes at both ends (source and receiver).

As a summary, the solution formulas for the reconstruction of the long-distance field are written in the following form:

$$U_z(r,z|\omega) = \frac{1}{2\pi}\sum_{m=-\infty}^{\infty}\int_0^{\infty} u_z^o(k,m,z,\omega)\omega^2 p J_m(\omega pr)d(pr),$$

(36)

$$U_r(r,z|\omega) = \frac{1}{2\pi}\sum_{m=-\infty}^{\infty}\int_0^{\infty} u_r^o(k,m,z,\omega)\omega^2 p \frac{d}{d(\omega pr)}J_m(\omega pr)d(pr),$$

(37)

$$U_\phi(r,z|\omega) = \frac{1}{2\pi}\sum_{m=-\infty}^{\infty}\int_0^{\infty} u_\phi^o(k,m,z,\omega)\frac{1}{r^2}\omega^2 \frac{d}{d(\omega pr)}J_m(\omega pr)d(pr).$$

(38)

where $u_z^o(k,m,z,\omega)$, $u_r^o(k,m,z,\omega)$, and $u_\phi^o(k,m,z,\omega)$ are the reflection-transmission coefficients obtained from the propagator matrix equation (33) and (35), and the physical parameters and boundary conditions are included. The symbol p represents the ray parameter, r is the distance source-receiver on the surface, and J_m is the Bessel function of the first kind and mth order. A second integration over ω (IFT) is applied to obtain the correspondent displacement, where it is necessary to calculate over a complete set of frequencies in the pass-band of the source pulse and fold over the real (even function) and imaginary (odd function) parts.

The source pulse $\mathbf{f} = \mathbf{f_E} = F(t,\mathbf{x})$ is conveniently separated in time and space factors, $F(t,\mathbf{x}) = F(t)F(\mathbf{x})$. The space factor is to localize the source by a Dirac delta function, $F(\mathbf{x}) = \delta(\mathbf{x}_0)$ at $\mathbf{x}_0$, where a

source directivity can be introduced. For the time factor there are several convenient functions like Ricker and Berlage, and a common time function used is given by:

$$F'(t) = \begin{cases} \sin(\delta t) - \frac{1}{m}\sin(m\delta t), & [\ 0 \le t \le T\ ], \\ 0, & [\ t < 0 \text{ and } t > T\ ], \end{cases} \tag{39}$$

where $\delta = \pi\frac{N}{T}$, $m = \frac{N+2}{N}$, $N = (1,2,\ldots)$. Typical values for the parameters are $N = 2$; $T = 30$ ms; $\Delta t = 4$ ms, corresponding to a Nyquist frequency of 125 Hz. The peak frequency of the pulse is around 35 Hz, and the spectral content above 100 Hz can be neglected [see Figs. 15 and 15] **Error! Reference source not found.**.

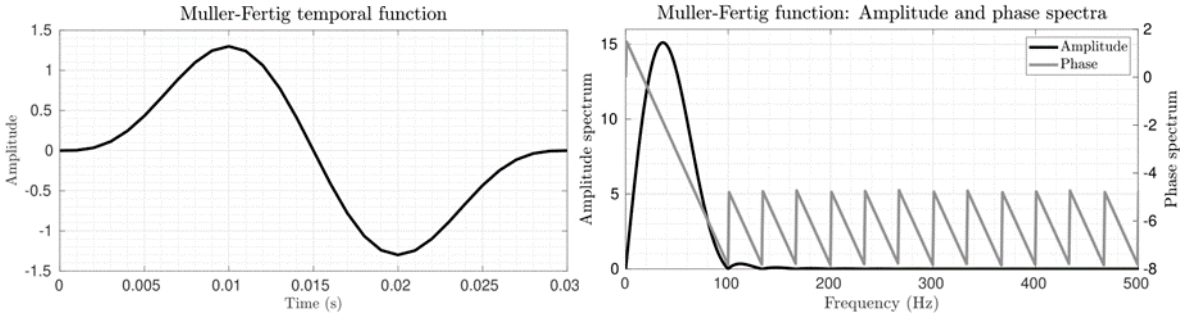

Figure 16: The Muller-Fertig temporal source function is represented by the equation (39), and its amplitude and phase spectra are plotted using the same frequency axis. (a) The parameters used were $T = 30$ ms and $N = 2$, which represent the dominant period and the number of extrema in the pulse. (b) Amplitude and phase spectra of the Muller-Fertig temporal function. In this example, most of the spectral content is below 100 Hz.

References

[1] Aki, K. And Richards, P. G. Quantitative Seismology. Theory And Methods. Volumes I And Ii.. W. H. Freeman And Company, New York, 1980.

[2] Alai, R. And Wapenaar, C. P. A. Pseudo Vsp Generation From Source Measurements: A New Tool For Seismic Interpretation. Journal Of Seismic Exploration, 3:79-94, 1994.

[3] Ameem, M. S. Fracture And In-Situ Stress Characterization Of Hydrocarbon Reservoirs. The Geological Society Of London, London, 2003.

[4] Andrade, F. T. B. And Leite, L. W. B. And Vieira, W. S. W. Pressure Prediction For A Block Of The Jequitinhonha Basin, Brazil. Brazilian Journal Of Geophysics, 38(3):21, 2020.

[5] Bernabini, M. And Carrion, P. And Jacovitti, G. And Rocca, F. And Treitel, S. And Worthington, M. H. Deconvolution And Inversion. Blackwell Scientific Publications, 1987.

[6] Biondi, L. B. 3d Seismic Imaging. Society Of Exploration Geophysicists, Tulsa, Ok, Usa, 2010.

[7] Carcione, J. M. And Poletto, F. Sound Velocity Of Drilling Mud Saturated With Reservoir Gas. Geophysics, 65(2):646-651, 2000.

[8] Davis, R. O. And Selvadurai, A. P. S. Elasticity And Geomechanics. Cambridge University Press, Cambridge, United Kingdom, 1996.

[9] Ferreira, A. D. S. Análise De Velocidade Na Estimativa Da Razão Gama Na Interpretação Vsp (In Portuguese). (Https://Cpgf.Propesp.Ufpa.Br/Index.Php/Br/Teses-E-Dissertacoes/Dissertacoes/281-2022). Master's Thesis, Universidade Federal Do Pará, Belém, Pa, Brazil, 2022.

[10] Fertig, J. And Muller, G. Computations Of Synthetic Seismograms For Caol Seams Of With The Reflectivity Method. Geophysical Prospecting, 26:868-88, 1978.

[11] Fomel, S. Velocity Analysis Using Ab Semblance. Geophysical Prospecting, 57:311-321, 2009.

[12] Galperin, E. I. Vertical Seismic Profiling And Its Exploration Potential. D. Reidel Publishing Company, Boston, 1985.

[13] Galperin, E. I. And Nersesov, I. L. And Galperina, R. M. Borehole Seismology And The Study Of The Seismic Regime Of Large Industrial Centres. D. Reidel Publishing Company, Boston, 1978.

[14] Gregory, A. R. Fluid Saturation Effect On Dynamic Elastic Properties Of Sedimentary Rocks. Geophysics, 41(5):895-921, 1976.

[15] Hantschel, T. And Kauerauf, A. I. Fundamentals Of Basin And Petroleum Systems Modeling. Springer-Verlag, Berlin, 2009.

[16] Hardage, B. A. An Examination Of Tube Wave Noise In Vertical Seismic Profiling Data. Geophysics, 46(6):982-903, 1981.

[17] Hardage, B. A. Vertical Seismic Profiling. Geophysical Press, Amsterdam, 1983.

[18] Hardage, B. A. And Deangelo, M. V. And Murray, P. E. And Sava, D. Multicomponent Seismic Technology. Society Of Exploration Geophysicists, Tulsa, Ok, Usa, 2011.

[19] Leite, L. W. B. And Vieira, W. W. S. Automatic Seismic Velocity Analysis Based On Nonlinear Optimization Of The Semblance Function. Journal Of Applied Geophysics, 161:182-192, 2019.

[20] Li, Y. And Hewett, B. Borehole Seismic Quantitative Diagnosis Of A Seismic Velocity Model For 3d Seismic Imaging Of Subsurface Structures. Geophysical Prospecting, :1-21, 2014.

[21] Ma, Y. And Loures, L. And Margrave, G. F. Seismic Modelling With The Reflectivity Method. Crewes Project, :1-7, 2004.

[22] Mann, J. Extensions And Applications Of The Common-Reflection-Surface Stack Method. Phd Thesis, Universitat Fridericiana Karlsruhe, 2002.

[23] Mattheij, R. M. M. And Rienstra, S. W. And Thije Boonkkamp, J. H. M. Partial Diffferential Equations. Modeling, Analysis, Computation. Siam, Philadelphia, 2005.

[24] Muller, G. The Reflectivity Method: A Tutorial. Journal Of Geophysics, 58:153-174, 1985.

[25] Nguyen Dac, T. And Sanders, M. And Millot, P. And Maula, F. And Rehman, S. And Nguyen, T. And Lawson, M. And Jeow, F. S. And Tran, K. Using Free Surface Vsp Downgoing Multiples To Obtain Unconventional Vsp Image Above The Well Trajectory - A Case Study. Apgce 2015 Www.Apgce.Com, (25516):1-5, 2015.
[26] Noris, A. N. The Speed Of A Tube Wave. J. Acoustic Soc. Am., 87(1):414-417, 1990.
[27] O'brian, J. And Harris, R. Multicomponent Vsp Imaging Of Tight-Gas Sands. Geophysics, 71(6):E83-E90, 2006.
[28] Owusu, J.C. And Podgornova, O. And Charara, M. And Leany, S. And Campbell, A. And Ali, S. And Borodin, I. And Nutt, L. And Menkiti, H. Anisotropic Elastic Full-Waveform Inversion Of Walkaway Vsp Data From The Arabian Gulf. Geophysical Prospecting, :1-16, 2015.
[29] Saada, A. S. Elasticity Theory And Applications. Pergamon Press Inc., New York, Ny, Usa, 1974.
[30] Sandmeier, K. J. Veranderung Und Erweiterung Des Reflektivitatsprogrames Zur Berechung Synthetischer Seismogramme. Master's Thesis, Karlsruhe Universitat. Geophysikalisches Institute., 1984.
[31] Seeman, B. And Horowicz, L. Vertical Seismic Profilling: Separation Of Upgoing And Downgoing Acoustic Waves In A Stratified Medium. Geophysics, 48(5):555-568, 1983.
[32] Sibiryakov, B. And Sibiriakov, E. And Leite, L. W. B. Dynamics Of Underground Rocks Containing Fluids. Application To Exploration Geophysics With Emphasis On Oil And Gas. Ufpa, Ig, Geosciences Library, Belém, Pará, Brazil, 2020.
[33] Soni, A. K. And Verschuur, D. J. Full-Wavefield Migration Of Vertical Seismic Profiling Data: Using All Multiples To Extend The Illumination Area. Geophysical Prospecting, :1-21, 2014.
[34] Steeghs, P. And Drijkoningen, G. Seismic Sequence Analysis And Attribute Extraction Using Quadratic Time-Frequency Representations. Geophysics, 66(6):1947-1959, 2001.
[35] Von Steht, M. 2d Co Crs Imaging For Multicomponent Data Recorded By The Vsp Geometry. Seg Annual Meeting, :3482-3486, 2006.
[36] Von Steht, M. Imaging Of Walkaway Vsp Data Using The Common-Reflection-Surface Stack. Phd Thesis, Universitat Fridericiana Karlsruhe, 2008.
[37] Von Steht, M. And Goertz, A. Imaging Walkaway Vsp Data Using The Common-Reflection-Surface Stack. The Leading Edge, :764-768, 2007.
[38] White, J. E. Underground Sound; Application Of Seismic Waves. Elsevier, Amsterdam, 1983.